Solitary waves bifurcated from Bloch-band edges in two-dimensional periodic media

Zuoqiang Shi[1] and Jianke Yang[2]
[1]*Zhou Pei-Yuan Center for Applied Mathematics, Tsinghua University, Beijing 100084, China*
[2]*Department of Mathematics and Statistics, University of Vermont, Burlington, Vermont 05401, USA*
(Received 23 January 2007; published 3 May 2007)

Solitary waves bifurcated from edges of Bloch bands in two-dimensional periodic media are determined both analytically and numerically in the context of a two-dimensional nonlinear Schrödinger equation with a periodic potential. Using multiscale perturbation methods, the envelope equations of solitary waves near Bloch bands are analytically derived. These envelope equations reveal that solitary waves can bifurcate from edges of Bloch bands under either focusing or defocusing nonlinearity, depending on the signs of the second-order dispersion coefficients at the edge points. Interestingly, at edge points with two linearly independent Bloch modes, the envelope equations lead to a host of solitary wave structures, including reduced-symmetry solitons, dipole-array solitons, vortex-cell solitons, and so on—many of which have not been reported before to our knowledge. It is also shown analytically that the centers of envelope solutions can be positioned at only four possible locations at or between potential peaks. Numerically, families of these solitary waves are directly computed both near and far away from the band edges. Near the band edges, the numerical solutions spread over many lattice sites, and they fully agree with the analytical solutions obtained from the envelope equations. Far away from the band edges, solitary waves are strongly localized, with intensity and phase profiles characteristic of individual families.

DOI: 10.1103/PhysRevE.75.056602 PACS number(s): 42.65.Tg, 05.45.Yv

I. INTRODUCTION

Nonlinear wave propagation in periodic media is attracting a lot of attention these days. This was stimulated in part by rapid advances in optics, Bose-Einstein condensates, and related fields. In optics, various periodic and quasi-periodic structures (such as photonic crystals, photonic crystal fibers, periodic waveguide arrays, and photonic lattices) have been constructed by ingenious experimental techniques, with applications to light routing, switching, and optical information processing [1–8]. These periodic media create a wide range of new phenomena for light propagation, even in the linear regime. For instance, the diffraction of light in a periodic medium exhibits distinctively different patterns from homogeneous diffraction [3]. If the periodic medium has a local defect, this defect can guide light by a totally new physical mechanism called repeated Bragg reflections [1,2,9–13]. When the nonlinear effects become significant, as with high-power beams or strongly nonlinear materials, the physical phenomena are even richer and more complex, and their understanding is far from complete yet. In Bose-Einstein condensates, one direction of recent research is to load the condensates into periodic optical lattices [14–16]. This problem and the above nonlinear optics problems are closely related, and are often analyzed together.

Solitary waves play an important role in nonlinear wave systems. These waves are nonlinear localized structures that propagate without change of shape. In the physical communities, they are often just called solitons, which we do occasionally in this paper as well. In one-dimensional (1D) periodic media, solitary waves (called lattice solitons) have been predicted and observed in optical experiments [3,8,17–20]. But in two and higher dimensions, periodic media can support a much wider array of solitary wave structures, many of which have no counterparts in 1D systems. So far, several types of 2D lattice solitons in the semi-infinite band gap (such as fundamental, dipole, and vortex solitons), as well as the first band gap (such as fundamental, vortex, and reduced-symmetry gap solitons), have been reported [5,15,21–31]. Solitons in Bessel-ring lattices and 2D quasiperiodic lattices have been reported as well [32–34]. All these works were either numerical or experimental, and an analytical understanding of these solitons is still lacking. Some of these solitons bifurcate from edges of Bloch bands. For instance, the gap vortex solitons reported in [27] bifurcate from the two X-symmetry points of the second Bloch band, and the reduced-symmetry solitons reported in [30] bifurcate from a single X-symmetry point of the second Bloch band (both under focusing nonlinearity). This raises the following important questions: Are there other types of solitary waves bifurcated from Bloch bands in 2D periodic media? How can such solitary waves be analytically predicted and classified?

In this paper, we determine all possible solitary-wave structures bifurcated from edges of Bloch bands in 2D periodic media both analytically and numerically, using the two-dimensional nonlinear Schrödinger equation with a periodic potential as the mathematical model. By multiscale perturbation methods, we derive the envelope equations of these solitary waves near band edges. We find that these envelope equations admit solutions that lead not only to solitons reported before (see [27,30] for instance), but also to additional solitary-wave structures such as dipole-array solitons bifurcated from the second Bloch band under focusing nonlinearity, and vortex-cell solitons bifurcated from the second Bloch band under *defocusing* nonlinearity. We also show analytically that the centers of envelope solutions can be positioned at only four possible locations at or between the potential peaks. We further determine directly using numerical methods whole families of these solitons both near and far away from band edges [35]. Near the band edges, the numerical solutions spread over many lattice sites, and they fully agree

 ©2007 The American Physical Society

with the analytical solutions obtained from the envelope equations. Far away from the band edges, solitary waves are strongly localized, and their intensities and phase profiles carry signatures of individual soliton families. These studies provide a rather complete understanding of solitary waves bifurcated from Bloch bands in 2D periodic media.

II. THE MATHEMATICAL MODEL

The mathematical model we use for the study of solitary waves in 2D periodic media is the 2D nonlinear Schrödinger (NLS) equation with a periodic potential:

$$iU_t + U_{xx} + U_{yy} - V(x,y)U + \sigma|U|^2U = 0, \tag{2.1}$$

where $U(x,y,t)$ is a complex function, $V(x,y)$ is the periodic potential (also called the lattice potential), and $\sigma = \pm 1$ is the sign of the nonlinearity. This model arises in Bose-Einstein condensates trapped in a 2D optical lattice (where t is time) [14,15], as well as in light propagation in a periodic Kerr medium under the paraxial approximation (where t is the distance of propagation). In certain optical materials (such as photorefractive crystals), the nonlinearity is of a different (saturable) type. But it is known that those different types of nonlinearities give qualitatively similar results to those for the Kerr nonlinearity above [21,24,25,36].

In this paper, we take the lattice potential as

$$V(x,y) = V_0(\sin^2 x + \sin^2 y), \tag{2.2}$$

whose periods L along the x and y directions are both equal to π. This square-lattice potential can be readily engineered in Bose-Einstein condensates [15,16] and optics [5,7]. This potential is separable, which makes our theoretical analysis a little easier. A similar analysis can be repeated for other types of periodic potentials and nonlinearities (such as saturable nonlinearities in photorefractive crystals [5,36]) with minimal changes. Without loss of generality, when we carry out specific computations, we always set $V_0=6$ in the potential (2.2).

Solitary waves in Eq. (2.1) are sought in the form

$$U(x,y,t) = u(x,y)e^{-i\mu t}, \tag{2.3}$$

where amplitude function $u(x,y)$ is a solution of the following equation:

$$u_{xx} + u_{yy} - [F(x) + F(y)]u + \mu u + \sigma|u|^2u = 0, \tag{2.4}$$

$$F(x) = V_0 \sin^2 x, \tag{2.5}$$

and μ is a propagation constant.

In this paper, we determine solitary waves in Eq. (2.4) which are bifurcated from the Bloch bands (i.e., continuous spectrum) of that equation. To do this, information about the Bloch bands of Eq. (2.4) is essential. Such Bloch bands will be analyzed first below.

III. BLOCH BANDS AND BAND GAPS

When the function $u(x,y)$ is infinitesimal, Eq. (2.4) becomes a linear equation:

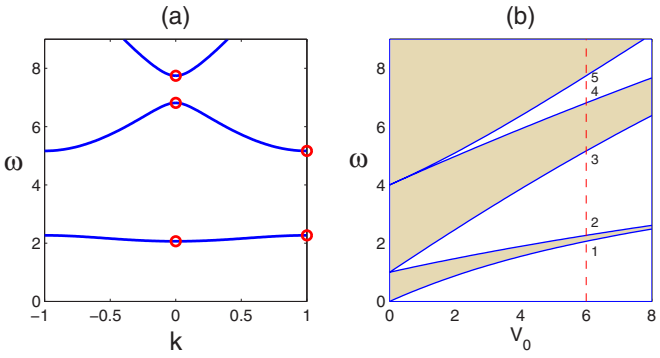

FIG. 1. (Color online) (a) Dispersion curves of the 1D equation (3.3) with $V_0=6$; (b) Bloch bands (shaded regions) and band gaps at various values of potential levels V_0 in Eq. (3.3). The circle points in (a) correspond to edges of Bloch bands marked by numbers 1–5 in (b). Bloch modes at these locations are displayed in Fig. 2.

$$u_{xx} + u_{yy} - [F(x) + F(y)]u + \mu u = 0. \tag{3.1}$$

Solutions of this linear equation are the Bloch modes, and the corresponding propagation constants μ form Bloch bands. Since the potential in (3.1) is separable, Bloch solutions and Bloch bands of this 2D equation can be constructed from solutions of a 1D equation. Specifically, the 2D Bloch solution $u(x,y)$ of Eq. (3.1) and its propagation constant μ can be split into the following form:

$$u(x,y) = p(x;\omega_a)p(y;\omega_b), \quad \mu = \omega_a + \omega_b, \tag{3.2}$$

where $p(x;\omega)$ is a solution of the following 1D equation:

$$p_{xx} - F(x)p + \omega p = 0. \tag{3.3}$$

This 1D equation is equivalent to Mathieu's equation. Its solution is

$$p(x;\omega) = e^{ikx}\tilde{p}(x;\omega), \tag{3.4}$$

where $\tilde{p}(x;\omega)$ is periodic with the same period π as the potential $F(x)$, and $\omega=\omega(k)$ is the 1D dispersion relation. This dispersion diagram is shown in Fig. 1(a) (for $V_0=6$). The band gap structure of this 1D equation (3.3) at various values of V_0 is shown in Fig. 1(b). Notice that, in the 1D case, at any nonzero value of V_0, band gaps appear; in addition, the number of band gaps is infinite. The first five Bloch waves $p(x;\omega_k)$, $1 \leqslant k \leqslant 5$, at the lowest five edges of Bloch bands $\omega=\omega_k$ are displayed in Fig. 2. These Bloch waves have been normalized to have unit amplitude. Notice that these solutions at band edges are all real valued.

Using these 1D dispersion results and the above connection between 1D and 2D Bloch solutions, we can construct the dispersion surfaces and band gap structures of the 2D problem (3.1). The 2D Bloch-mode solution is of the form

$$u(x,y) = e^{ik_x x + ik_y y}\tilde{p}[x;\omega(k_x)]\tilde{p}[y;\omega(k_y)], \tag{3.5}$$

where

$$\mu = \omega(k_x) + \omega(k_y), \quad -1 \leqslant k_x, k_y \leqslant 1, \tag{3.6}$$

is the 2D dispersion relation, and $-1 \leqslant k_x, k_y \leqslant 1$ is the first Brillouin zone. This 2D dispersion relation (at $V_0=6$) is

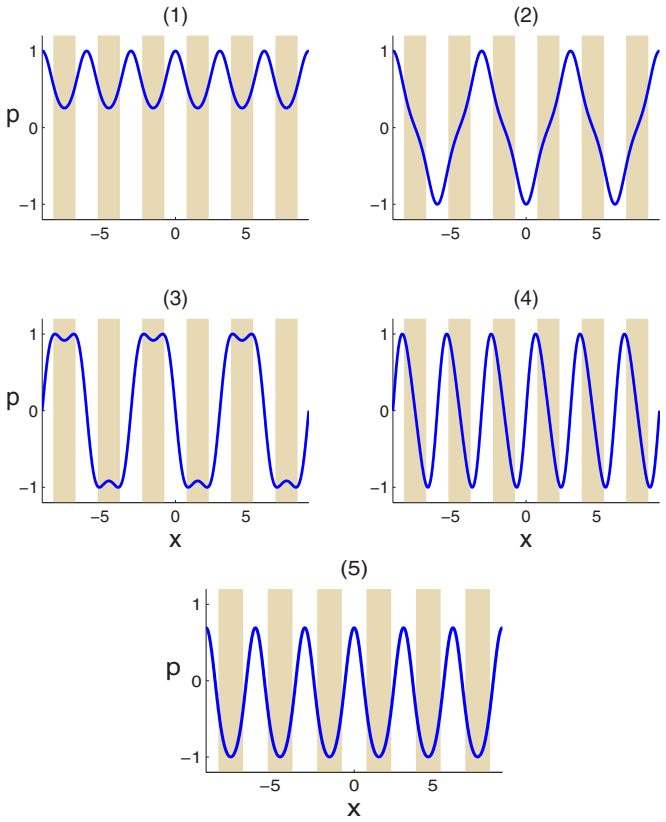

FIG. 2. (Color online) One-dimensional Bloch waves of Eq. (3.3) at the lowest five edges of the Bloch bands marked by circles in Fig. 1(a) and by numbers in Fig. 1(b). (1) $\omega_1=2.063\,182$; (2) $\omega_2=2.266\,735$; (3) $\omega_3=5.165\,940$; (4) $\omega_4=6.814\,29$; (5) $\omega_5=7.746\,78$.

shown in Fig. 3(a). The 2D band gap structure at various values of V_0 is shown in Fig. 3(b). Unlike the 1D case, for a given V_0 value, there are only a finite number of band gaps in the 2D problem. The first band gap appears only when $V_0>1.40$, the second band gap appearing when $V_0>4.13$, etc. As V_0 increases further, more band gaps will be found. At the potential strength $V_0=6$ as used in this paper, two band gaps exist. The edges of Bloch bands at this V_0 value are marked in Fig. 3(b) as A, B, C, D, E, respectively.

The locations of Bloch-band edges in the first Brillouin zone are important, as these locations reveal the symmetry properties of Bloch modes. To clearly mark such locations, we plotted the first Brillouin zone in Fig. 3. In the literature, the center of this Brillouin zone is called the Γ point, the four corners are called the M points, and points $(k_x,k_y)=(1,0),(0,1)$ are called the X and X' points, respectively [27]. These points are marked in the Brillouin zone of Fig. 3. Note that the four corner (M) points correspond to the same Bloch mode, but points X and X' lead to different (linearly independent) Bloch modes. In this first Brillouin zone, the Bloch-band edges A and B in Fig. 3(b) are located at the Γ and M symmetry points, respectively. At band edge C, there are two points on the dispersion surfaces which are located at the X and X' symmetry points. The same goes for the band edge D. The band edge E is located at the Γ symmetry point.

Now we examine 2D Bloch solutions at band edges. To illustrate, we consider the edge points A, B, C, D, and E in Fig. 3(b), where $V_0=6$. At both points A and B, there is a single Bloch solution. The Bloch solution at point A (located at the Γ point of the Brillouin zone) is $u(x,y)=p(x;\omega_1)p(y;\omega_1)$, where $p(x;\omega_1)$ is shown in Fig. 2(1). This solution is displayed in Fig. 4(a). Its propagation constant is $\mu=2\omega_1$. Notice that this solution has the symmetry $u(x,y)=u(y,x)$. For convenience, we denote point A as 1+1, and it is so indicated in Fig. 3(b). Similarly, the Bloch solution at point B (located at the M point of the Brillouin zone) is $u(x,y)=p(x;\omega_2)p(y;\omega_2)$, where $p(x;\omega_2)$ is shown in Fig. 2(2). This solution is displayed in Fig. 4(b), and its propagation constant is $\mu=2\omega_2$. This solution has the symmetry $u(x,y)=u(y,x)$ as well. Point B is 2+2 in our notations. Points C, D, and E are different from A and B and are more interesting. At these points, there are *two* linearly independent Bloch solutions, $u(x,y)$ and $u(y,x)$. At point C, these two solutions are $u(x,y)=p(x;\omega_1)p(y;\omega_3)$ and $u(y,x)=p(y;\omega_1)p(x;\omega_3)$, with the same propagation constant $\mu=\omega_1+\omega_3$. Here $p(x;\omega_3)$ is shown in Fig. 2(3). These solutions correspond to the X and X' points in the Brillouin zone. Point C is thus 1+3. Its $u(x,y)$ solution is displayed in Fig. 4(c); the $u(y,x)$ solution is just a 90° rotation of $u(x,y)$ in Fig. 4(c) and thus not shown. Point D is 2+4, where the two linearly independent Bloch solutions are $u(x,y)$

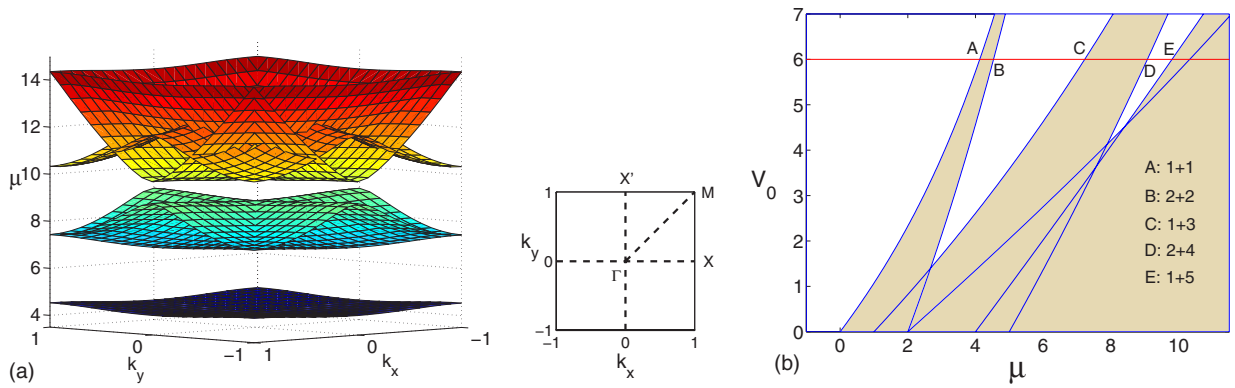

FIG. 3. (Color online) (a) Dispersion surfaces of the 2D problem (3.1) at $V_0=6$; the small figure at its side is the first Brillouin zone; (b) the 2D band gap structure for various values of V_0. Letters A, B, C, D, E mark the edges of Bloch bands at $V_0=6$. Insets like A:1+1 are explained in the text.

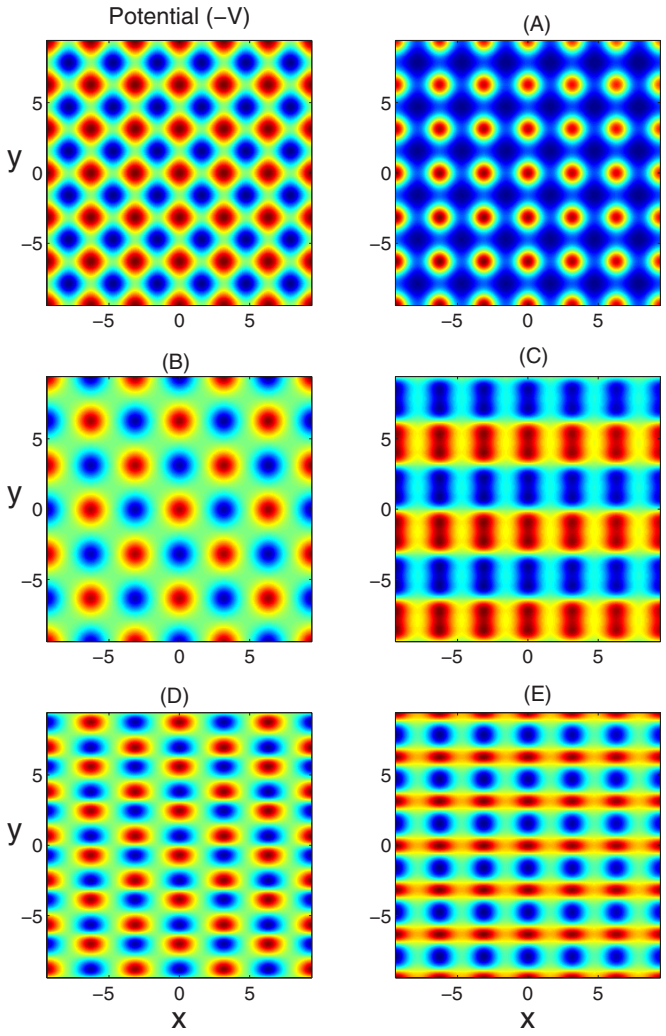

FIG. 4. (Color online) Upper left: the potential function $-V(x,y)$; (A), (B), (C), (D), and (E) are Bloch modes at the edge points of Bloch bands marked by the same letters in Fig. 3(b).

$=p(x;\omega_2)p(y;\omega_4)$ and $u(y,x)=p(y;\omega_2)p(x;\omega_4)$, the former of which is displayed in Fig. 4(d). These solutions also correspond to the X and X' points in the Brillouin zone. Point E is $1+5$, and the two Bloch solutions are $u(x,y)=p(x;\omega_1)p(y;\omega_5)$ and $u(y,x)=p(y;\omega_1)p(x;\omega_5)$ [the former is shown in Fig. 4(e)]. These solutions correspond to the Γ symmetry point in the Brillouin zone. It is interesting that, at point E, the two different Bloch modes are both located at the same Γ point, while at points C and D, the two Bloch modes are located at different symmetry points (X and X') in the Brillouin zone. This difference between points E and {C, D} will manifest itself later in solitary-wave bifurcations. Because of the existence of two linearly independent Bloch solutions at band edges C, D, and E, their linear superpositions remain a solution. These superpositions can give rise to interesting solution patterns, some of which (such as vortex arrays) have been pointed out before [12,27], while many others have not, to our knowledge. Solitary waves bifurcated from these linearly superimposed Bloch modes represent one of the subjects we will focus on in the remainder of the paper.

The above Bloch solutions exist on band edges with infinitesimal amplitudes. When the amplitudes of these solutions increase, these Bloch solutions may localize and form solitary-wave structures. The corresponding propagation constant μ then moves from band edges into band gaps. In the next section, we analyze how solitary waves bifurcate from Bloch solutions of band edges using multiscale perturbation methods.

IV. ENVELOPE EQUATIONS OF BLOCH MODES

In this section, we develop an asymptotic theory to analyze small-amplitude solitary waves bifurcating from Bloch waves near band edges in Eq. (2.4), and derive their envelope equations. We know that at an edge of a Bloch band there may be either one or two linearly independent Bloch modes. The bifurcation analyses for these two cases are similar; thus we will present detailed calculations only for the latter case (which is a little more complex), and just give the results for the former case.

A. Derivation of envelope equations

Let us consider a 2D band edge $\mu_0=\omega_{0,1}+\omega_{0,2}$, where $\omega_{0,n}$ $(n=1,2)$ are 1D band edges, $\omega_{0,1}\neq\omega_{0,2}$, and the two linearly independent Bloch modes are $p_1(x)p_2(y)$ and $p_1(y)p_2(x)$ with $p_n(x)=p(x;\omega_{0,n})$. Notice that

$$p_n(x+L)=\pm p_n(x) \tag{4.1}$$

since $\omega_{0,n}$ is a 1D band edge. Here $L=\pi$ is the period of the 1D potential $F(x)$. When the solution $u(x,y)$ of Eq. (2.4) is infinitesimally small, this solution on the band edge is then a linear superposition of these two Bloch modes in the general case. When $u(x,y)$ is small but not infinitesimal, we can expand the solution $u(x,y)$ of (2.4) into a multiscale perturbation series:

$$u=\epsilon u_0+\epsilon^2 u_1+\epsilon^3 u_2+\cdots, \tag{4.2}$$

$$\mu=\mu_0+\eta\epsilon^2, \tag{4.3}$$

where

$$u_0=A_1(X,Y)p_1(x)p_2(y)+A_2(X,Y)p_2(x)p_1(y), \tag{4.4}$$

$\eta=\pm 1$, and $X=\epsilon x$, $Y=\epsilon y$ are the long spatial scales of the envelope functions A_1 and A_2. Substituting the above expansions into Eq. (2.4), the equation at $O(\epsilon)$ is automatically satisfied. At order $O(\epsilon^2)$, the equation for u_1 is

$$u_{1xx}+u_{1yy}-[F(x)+F(y)]u_1+\mu_0 u_1=-2\left(\frac{\partial^2 u_0}{\partial x\partial X}+\frac{\partial^2 u_0}{\partial y\partial Y}\right). \tag{4.5}$$

Its homogeneous equation has two linearly independent solutions, $p_1(x)p_2(y)$, and $p_1(y)p_2(x)$. In order for the inhomogeneous equation (4.5) to admit a solution, the Fredholm conditions

$$\int_0^{2L}\int_0^{2L}\left(\frac{\partial^2 u_0}{\partial x\partial X}+\frac{\partial^2 u_0}{\partial y\partial Y}\right)p_1(x)p_2(y)dx\,dy=0, \tag{4.6}$$

$$\int_0^{2L}\int_0^{2L}\left(\frac{\partial^2 u_0}{\partial x\partial X}+\frac{\partial^2 u_0}{\partial y\partial Y}\right)p_2(x)p_1(y)dx\,dy=0 \quad (4.7)$$

must be satisfied. Here the integration length is $2L$ rather than L since the homogeneous solutions $p_1(x)p_2(y)$ and $p_2(x)p_1(y)$ may have periods $2L$ along the x and y directions [see Eq. (4.1)]. Recalling the u_0 solution (4.4), it is easy to check that the above Fredholm conditions are indeed satisfied automatically; thus, we can find a solution for Eq. (4.5) as

$$u_1=\frac{\partial A_1}{\partial X}\nu_1(x)p_2(y)+\frac{\partial A_1}{\partial X}\nu_2(y)p_1(x)+\frac{\partial A_2}{\partial X}\nu_2(x)p_1(y)+\frac{\partial A_2}{\partial X}\nu_1(y)p_2(x), \quad (4.8)$$

where $\nu_n(x)$ is a periodic solution of the equation

$$\nu_{n,xx}-F(x)\nu_n+\omega_{0,n}\nu_n=-2p_{n,x},\quad n=1,2. \quad (4.9)$$

At $O(\epsilon^3)$, the equation for u_2 is

$$u_{2xx}+u_{2yy}-[F(x)+F(y)]u_2+\mu_0 u_2=-\left(2\frac{\partial^2 u_1}{\partial x\partial X}+2\frac{\partial^2 u_1}{\partial y\partial Y}+\frac{\partial^2 u_0}{\partial X^2}+\frac{\partial^2 u_0}{\partial Y^2}+\eta u_0+|u_0|^2u_0\right). \quad (4.10)$$

Substituting the formulas (4.4) and (4.8) for u_0 and u_1 into this equation, we get

$$\begin{aligned}-\{u_{2xx}+u_{2yy}-[F(x)+F(y)]u_2+\mu_0u_2\}&=\frac{\partial^2A_1}{\partial X^2}[2\nu_1'(x)+p_1(x)]p_2(y)+\frac{\partial^2A_1}{\partial Y^2}[2\nu_2'(y)+p_2(y)]p_1(x)+\frac{\partial^2A_2}{\partial X^2}[2\nu_2'(x)+p_2(x)]p_1(y)\\&+\frac{\partial^2A_2}{\partial Y^2}[2\nu_1'(y)+p_1(y)]p_2(x)+2\frac{\partial^2A_1}{\partial X\partial Y}[p_1'(x)\nu_2(y)+p_2'(y)\nu_1(x)]+2\frac{\partial^2A_2}{\partial X\partial Y}[p_2'(x)\nu_1(y)\\&+p_1'(y)\nu_2(x)]+p_1^3(x)p_2^3(y)|A_1|^2A_1+p_1(x)p_2(y)p_1^2(y)p_2^2(x)(\bar{A}_1A_2^2+2A_1|A_2|^2)\\&+p_2^3(x)p_1^3(y)|A_2|^2A_2+p_1^2(x)p_2^2(y)p_1(y)p_2(x)(\bar{A}_2A_1^2+2A_2|A_1|^2)+\eta A_1(X,Y)p_1(x)p_2(y)\\&+\eta A_2(X,Y)p_2(x)p_1(y). \end{aligned} \quad (4.11)$$

Here the overbar represents complex conjugation. Before applying the Fredholm conditions to this inhomogeneous equation, we notice the following identities:

$$\int_0^{2L}p_1(x)p_2(x)dx=0, \quad (4.12)$$

$$\int_0^{2L}p_1(x)\nu_2(x)dx=\int_0^{2L}p_2(x)\nu_1(x)dx, \quad (4.13)$$

and

$$\int_0^{2L}[2\nu_n'(x)+p_n(x)]p_n(x)dx=D_n\int_0^{2L}p_n^2(x)dx,\quad n=1,2, \quad (4.14)$$

where

$$D_n\equiv\left.\frac{1}{2}\frac{d^2\omega}{dk^2}\right|_{\omega=\omega_{0,n}}. \quad (4.15)$$

The identity (4.12) holds since $p_1(x)$ and $p_2(x)$ are the eigenfunctions of the self-adjoint linear Schrödinger operator with different eigenvalues. The identity (4.13) can be confirmed by taking the inner product between Eq. (4.9) and the functions $p_n(x)$. The identity (4.14) can be verified by expanding the solution of Eq. (3.3) around the edge of the Bloch band $\omega=\omega_{0,n}$ [see Eq. (15) in [20]]. Utilizing these identities and (4.1), the Fredholm conditions for Eq. (4.11) finally lead to the following coupled nonlinear equations for the envelope functions A_1 and A_2:

$$D_1\frac{\partial^2A_1}{\partial X^2}+D_2\frac{\partial^2A_1}{\partial Y^2}+\eta A_1+\sigma[\alpha|A_1|^2A_1+\beta(\bar{A}_1A_2^2+2A_1|A_2|^2)+\gamma(|A_2|^2A_2+\bar{A}_2A_1^2+2A_2|A_1|^2)]=0, \quad (4.16)$$

$$D_2\frac{\partial^2A_2}{\partial X^2}+D_1\frac{\partial^2A_2}{\partial Y^2}+\eta A_2+\sigma[\alpha|A_2|^2A_2+\beta(\bar{A}_2A_1^2+2A_2|A_1|^2)+\gamma(|A_1|^2A_1+\bar{A}_1A_2^2+2A_1|A_2|^2)]=0. \quad (4.17)$$

Here

$$\alpha=\frac{\int_0^{2L}\int_0^{2L}p_1^4(x)p_2^4(y)dx\,dy}{\int_0^{2L}\int_0^{2L}p_1^2(x)p_2^2(y)dx\,dy}, \quad (4.18)$$

$$\beta = \frac{\int_0^{2L}\int_0^{2L} p_1^2(x)p_2^2(x)p_1^2(y)p_2^2(y)dx\,dy}{\int_0^{2L}\int_0^{2L} p_1^2(x)p_2^2(x)dx\,dy}, \quad (4.19)$$

and

$$\gamma = \frac{\int_0^{2L}\int_0^{2L} p_1^3(x)p_2(x)p_2^3(y)p_1(y)dx\,dy}{\int_0^{2L}\int_0^{2L} p_1^2(x)p_2^2(y)dx\,dy}. \quad (4.20)$$

Notice that α and β are always positive, but γ may be positive, negative, or zero.

The coefficients in Eqs. (4.16) and (4.17) can be readily determined from Bloch solutions of the 1D equation (3.3). In particular, when the 1D Bloch waves $p_1(x)$ and $p_2(x)$ have been normalized to have unit amplitude (see Fig. 2), we find that at point C,

$$D_1 = 0.434\,845, \quad D_2 = 2.422\,196, \quad \alpha = 0.5821, \quad \beta = 0.1325, \quad \gamma = 0; \quad (4.21)$$

at point D,

$$D_1 = -0.586\,799, \quad D_2 = -13.264\,815, \quad \alpha = 0.5256, \quad \beta = 0.1811, \quad \gamma = 0; \quad (4.22)$$

and at point E,

$$D_1 = 0.434\,845, \quad D_2 = 15.793\,172, \quad \alpha = 0.4684, \quad \beta = 0.0781, \quad \gamma = -0.0261. \quad (4.23)$$

At band edges where a single Bloch mode exists [such as points A and B in Fig. 3(b)], the envelope equation for this single Bloch mode can be more easily derived. In this case, this single Bloch mode must be of the form $p_1(x)p_1(y)$, where $p_1(x)=p(x;\omega_{0,1})$, and $\omega_{0,1}$ is a band edge in the 1D problem (3.3). Unlike the previous case, interchanging x and y of this Bloch solution does not give different Bloch modes. The leading order solution $u_0(x,y)$ in the expansion (4.2) now is $A_1(X,Y)p_1(x)p_1(y)$, and the envelope equation for $A_1(X,Y)$ can be found to be

$$D_1\left(\frac{\partial^2 A_1}{\partial X^2} + \frac{\partial^2 A_1}{\partial Y^2}\right) + \eta A_1 + \sigma\alpha_0|A_1|^2 A_1 = 0, \quad (4.24)$$

where D_1 is as given in Eq. (4.15), and

$$\alpha_0 = \frac{\int_0^{2L}\int_0^{2L} p_1^4(x)p_1^4(y)dx\,dy}{\int_0^{2L}\int_0^{2L} p_1^2(x)p_1^2(y)dx\,dy}. \quad (4.25)$$

In particular, when the Bloch solution $p_1(x)$ is normalized to have unit amplitude, then at point A

$$D_1 = 0.434\,845, \quad \alpha_0 = 0.462\,815; \quad (4.26)$$

and at point B,

$$D_1 = -0.588\,073, \quad \alpha_0 = 0.500\,922. \quad (4.27)$$

We note that, for this single-Bloch-mode case, an envelope equation similar to (4.24) has been derived before in [37].

B. Locations of envelope solitons

The envelope equations (4.16), (4.17), and (4.24) are translation invariant. For instance, if $[A_1(X,Y),A_2(X,Y)]$ is a solution of Eqs. (4.16) and (4.17), so is $[A_1(X-X_0,Y-Y_0),A_2(X-X_0,Y-Y_0)]$, where (X_0,Y_0) are any constants. However, only when (X_0,Y_0) take some special values can the perturbation series solution (4.2) truly satisfy the original equation (2.4). The reason is that (X_0,Y_0) must satisfy certain additional constraints. These constraints are exponentially small in ϵ; thus, they cannot be captured in the power series expansions of (4.2), but need to be calculated using asymptotics beyond all orders techniques [38] or other equivalent methods [20]. In 1D problems, it has been shown that envelope solitons can be located only at two positions relative to the periodic lattice [20] (or the underlying periodic wave train [38]). In the present 2D problem, we will show below that envelope solitons can be located only at four positions relative to the 2D periodic lattice by a method similar to that used in [20]. As we have done in the previous subsection, detailed derivations will be presented for the (A_1,A_2) solutions of Eqs. (4.16) and (4.17). Similar results hold for the A_1 solution of Eq. (4.24) as well.

First we derive two constraints for the envelope solutions. Multiplying Eq. (2.4) by $\bar{u}_x$ or $\bar{u}_y$, adding its conjugate equation, and integrating from $-\infty$ to $+\infty$, we get the following two constraints:

$$\int_{-\infty}^{+\infty}\int_{-\infty}^{+\infty} F'(x)|u(x,y)|^2 dx\,dy = 0, \quad (4.28)$$

$$\int_{-\infty}^{+\infty}\int_{-\infty}^{+\infty} F'(y)|u(x,y)|^2 dx\,dy = 0. \quad (4.29)$$

Substituting the perturbation expansion (4.2) of the solution $u(x,y)$ into the above equations, these constraints at the leading order become

$$I_1(x_0,y_0) = \epsilon^2\int_{-\infty}^{+\infty}\int_{-\infty}^{+\infty} F'(x)|A_1p_1(x)p_2(y) + A_2p_2(x)p_1(y)|^2 dx\,dy = 0, \quad (4.30)$$

$$I_2(x_0,y_0) = \epsilon^2\int_{-\infty}^{+\infty}\int_{-\infty}^{+\infty} F'(y)|A_1p_1(x)p_2(y) + A_2p_2(x)p_1(y)|^2 dx\,dy = 0. \quad (4.31)$$

Here

$$A_k = A_k(X - X_0, Y - Y_0), \quad k = 1,2, \tag{4.32}$$

and $(X_0, Y_0) = (\epsilon x_0, \epsilon y_0)$ is the center position of the envelope solution (A_1, A_2). In this paper, we consider envelope functions (A_1, A_2) such that $|A_1|^2$, $|A_2|^2$, and $A_1\bar{A}_2 + \bar{A}_1 A_2$ are symmetric in X and Y about the center position (X_0, Y_0), i.e.,

$$|A_k(-X,Y)|^2 = |A_k(X,Y)|^2 = |A_k(X,-Y)|^2, \quad k = 1,2, \tag{4.33}$$

and similar relations hold for $A_1\bar{A}_2 + \bar{A}_1 A_2$. All solitary-wave solutions of Eqs. (4.16) and (4.17) that we know satisfy these assumptions (up to spatial translations).

Now we examine the constraint (4.30). This constraint can be rewritten as

$$\begin{aligned} I_1(x_0,y_0) = \epsilon^2 \int_{-\infty}^{+\infty} \int_{-\infty}^{+\infty} F'(x)[|A_1|^2 p_1^2(x) p_2^2(y) \\ + |A_2|^2 p_2^2(x) p_1^2(y) + (A_1 \bar{A}_2 \\ + \bar{A}_1 A_2) p_1(x) p_2(x) p_1(y) p_2(y)] dx\, dy = 0. \end{aligned} \tag{4.34}$$

Since $F'(x)$ is antisymmetric and $p_1^2(x), p_2^2(x)$ both symmetric, the functions $F'(x)p_1^2(x)p_2^2(y)$, $F'(x)p_2^2(x)p_1^2(y)$, and $F'(x)p_1(x)p_2(x)p_1(y)p_2(y)$ have the following Fourier series expansions:

$$F'(x)p_1^2(x)p_2^2(y) = \sum_{m=1}^{\infty} \sum_{n=0}^{\infty} c_{m,n}^{(1)} \sin \frac{2\pi m x}{L} \cos \frac{2\pi n y}{L}, \tag{4.35}$$

$$F'(x)p_2^2(x)p_1^2(y) = \sum_{m=1}^{\infty} \sum_{n=0}^{\infty} c_{m,n}^{(2)} \sin \frac{2\pi m x}{L} \cos \frac{2\pi n y}{L}, \tag{4.36}$$

$$\begin{aligned} F'(x)p_1(x)p_2(x)p_1(y)p_2(y) \\ = \sum_{m=1}^{\infty} \sum_{n=0}^{\in fty} c_{m,n}^{(3)} \sin \frac{2\pi m x}{L} \cos \frac{2\pi n y}{L} \\ + \sum_{m=0}^{\infty} \sum_{n=1}^{\infty} d_{m,n}^{(3)} \cos \frac{2\pi m x}{L} \sin \frac{2\pi n y}{L}. \end{aligned} \tag{4.37}$$

Here $d_{m,n}^{(3)} = 0$ or $c_{m,n}^{(3)} = 0$ (for all m,n) if $p_1(x)p_2(x)$ is even or odd, respectively. When the above Fourier expansions are substituted into Eq. (4.34), every Fourier mode in these expansions leads to an exponentially small term in (4.34), and the exponential rate of decay of these terms is larger for higher values of $m+n$. Keeping only the leading-order term obtained from Fourier modes with $m+n=1$, Eq. (4.34) becomes

$$\begin{aligned} I_1(x_0,y_0) = \epsilon^2 \int_{-\infty}^{+\infty} \int_{-\infty}^{+\infty} \Big([c_{1,0}^{(1)} |A_1|^2 + c_{1,0}^{(2)} |A_2|^2 \\ + c_{1,0}^{(3)} (A_1 \bar{A}_2 + \bar{A}_1 A_2)] \sin \frac{2\pi x}{L} \\ + d_{1,0}^{(3)} (A_1 \bar{A}_2 + \bar{A}_1 A_2) \sin \frac{2\pi y}{L} \Big) dx\, dy. \end{aligned} \tag{4.38}$$

Recalling Eq. (4.32) and our symmetry assumptions on $|A_1|^2$, $|A_2|^2$, and $A_1\bar{A}_2 + \bar{A}_1 A_2$ [see (4.33)], the above integral can be simplified to be

$$I_1(x_0,y_0) = W_{1,1} \sin(2\pi x_0/L) + W_{1,2} \sin(2\pi y_0/L), \tag{4.39}$$

where

$$\begin{aligned} W_{1,1} \equiv \epsilon^2 \int_{-\infty}^{+\infty} \int_{-\infty}^{+\infty} \{ c_{1,0}^{(1)} |A_1(X,Y)|^2 \\ + c_{1,0}^{(2)} |A_2(X,Y)|^2 + c_{1,0}^{(3)} [A_1(X,Y) \bar{A}_2(X,Y) \\ + \bar{A}_1(X,Y) A_2(X,Y)] \} \cos \frac{2\pi x}{L} dx\, dy \end{aligned} \tag{4.40}$$

and

$$\begin{aligned} W_{1,2} \equiv \epsilon^2 \int_{-\infty}^{+\infty} \int_{-\infty}^{+\infty} d_{1,0}^{(3)} [A_1(X,Y) \bar{A}_2(X,Y) \\ + \bar{A}_1(X,Y) A_2(X,Y)] \cos \frac{2\pi y}{L} dx\, dy. \end{aligned} \tag{4.41}$$

Notice that both integrals $W_{1,2}$ and $W_{1,2}$ are exponentially small in ϵ; thus, the constraint (4.30) is exponentially small and hence cannot be captured by the power-series perturbation expansions (4.2). Repeating similar calculations for the integral of $I_2(x_0,y_0)$ in Eq. (4.31), we can get (to the leading order)

$$I_2(x_0,y_0) = W_{2,1} \sin(2\pi x_0/L) + W_{2,2} \sin(2\pi y_0/L), \tag{4.42}$$

where the expressions for $W_{2,1}$ and $W_{2,2}$ are similar to those for $W_{1,1}$ and $W_{1,2}$ above. Then in order for the two constraints (4.30) and (4.31) to hold, we must have

$$\sin(2\pi x_0/L) = \sin(2\pi y_0/L) = 0. \tag{4.43}$$

Thus, the envelope solution (A_1, A_2) can be centered at only four locations:

$$(x_0,y_0) = (0,0), \left(0, \frac{L}{2}\right), \left(\frac{L}{2}, 0\right), \left(\frac{L}{2}, \frac{L}{2}\right). \tag{4.44}$$

Note that, due to the x and y symmetry of the lattice, envelope solutions centered at the second and third locations as above are topologically the same (except for an interchange of x and y axes). Other possible locations of (x_0,y_0), such as (L,L), are equivalent to one of the four locations above due to the periodicity of the lattice potential.

V. SOLUTIONS OF ENVELOPE EQUATIONS

The envelope equations (4.16), (4.17), and (4.24) are some of the key results of this paper. They have important consequences. First, they show that solitary waves are possible only when $\eta D_1<0$ and $\eta D_2<0$. This simply means that μ must lie in the band gap of the linear system see [Eq. (4.3)]. Second, these equations show that solitary waves exist only when the dispersion coefficients D_1, D_2 and the nonlinearity coefficient σ are of the same sign. For instance, at points A, C, and E in Fig. 3, where $D_1>0$ and $D_2>0$, solitary waves exist only when $\sigma>0$, i.e., for focusing nonlinearity, but not for defocusing nonlinearity ($\sigma<0$). The situation is opposite at points B and D. This result is consistent with our physical intuition, as well as the 2D experimental observations in [31].

Below, we consider soliton solutions of the envelope equations (4.24), (4.16), and (4.17). The scalar equation (4.24) is the familiar 2D NLS equation, and it admits the following types of solitary wave solutions: (1) $A_1=f(R)$, which is real and radially symmetric; here (R,Θ) is the polar coordinates of (X,Y); and (2) $A_1=f(R)e^{in\Theta}$, where n is an integer; this is a vortex-ring solution with charge n.

The coupled envelope equations (4.16) and (4.17) admit a wider array of solutions. A complete classification of their solutions is beyond the scope of the present paper. Below we list only a few types of their solutions. If $\gamma=0$, these equations admit the following three simple solution reductions.

(i) $A_1\neq 0$, $A_2=0$; or $A_1=0$, $A_2\neq 0$. In this case, the solution is a single Bloch-wave envelope solution. Notice that A_1 (or A_2) satisfies a 2D NLS equation with different dispersion coefficients D_1 and D_2 along the X and Y directions; thus, these solutions are simply those described above (charge-free or vortex solutions) except for being stretched along the X or Y direction and hence becoming ellipse shaped.

(ii) $A_1, A_2\in\mathbb{R}$, where $\mathbb{R}$ is the set of real numbers. In this case, the solution is a real-valued vector envelope state. Note that, if $(A_1,A_2)\in\mathbb{R}$ is a solution, so are $(-A_1,A_2)$, $(A_1,-A_2)$, $(-A_1,-A_2)$, and (iA_1,iA_2). All these solutions are equivalent to each other and lead to the equivalent solitary waves in the original system (2.4).

(iii) $A_1\in\mathbb{R}, A_2\in i\mathbb{R}$. In this case, the solution is a complex-valued vector envelope state. Note that the other solution of $A_1\in i\mathbb{R}, A_2\in\mathbb{R}$ is equivalent to this $A_1\in\mathbb{R}, A_2\in i\mathbb{R}$ solution.

If $\gamma\neq 0$, however, the reductions are quite different. For instance, the first and third reductions of case $\gamma=0$ no longer hold. In this case, the reduction of $A_1, A_2\in\mathbb{R}$ is allowed. Under this reduction, there are two subcases, $A_1>0$, $A_2>0$, and $A_1>0$, $A_2<0$, which are *not* equivalent to each other. They lead to different solitary waves in Eq. (2.4) (see the end of this section).

It is noteworthy that at band edges where $\gamma\neq 0$, the single Bloch-wave envelope reductions of $A_1\neq 0$, $A_2=0$ and $A_1=0$, $A_2\neq 0$ are not possible. Physically, this is due to a resonance between the two Bloch modes, which prevents the existence of a single-Bloch-mode envelope solution. For instance, at point E of Fig. 3 where $\gamma\neq 0$ [see Eq. (4.23)], the two Bloch modes are both located at the same Γ point in the first Brillouin zone [see Sec. III and Fig. 4(e)]. These two Bloch modes are thus in resonance, which makes $\gamma\neq 0$. At points where $\gamma=0$ (such as points C and D in Fig. 3), the two Bloch solutions are located at different symmetry points of the Brillouin zone and are not in resonance; thus single-Bloch-wave reductions of $A_1\neq 0$, $A_2=0$ and $A_1=0$, $A_2\neq 0$ are possible there.

To illustrate various envelope-soliton solutions admitted by Eqs. (4.24), (4.16), and (4.17), we consider points A, B, C, D, and E of Fig. 3 in detail below. At each of these five points, we determine solutions of the underlying envelope equations. For each envelope solution, we also display the corresponding leading-order analytical solution $u_0(x,y)$. Since envelope solitons can have four different locations (see the previous section), which will lead to four different solutions $u_0(x,y)$, for simplicity, we will display only the one where the envelope is centered at $(x_0,y_0)=(0,0)$ below.

First we consider point A. At this point, a single Bloch mode exists and has been shown in Fig. 4(a). This Bloch wave is located at the Γ point of the first Brillouin zone, is π periodic along both x and y directions, and is all positive. The envelope equation at this point is given by (4.24) with the coefficients D_1 and α_0 given in Eq. (4.26). Since $D_1>0$, solitary waves will bifurcate into the semi-infinite band gap ($\eta<0$) under a focusing nonlinearity ($\sigma=1$). If we take the solution of (4.24) to be $A_1=f(R)$ where $f(R)>0$ is the ground-state envelope solution, the corresponding leading-order analytical solution $u_0(x,y)$ is a nodeless solitary wave. Such solutions have been reported before [5,7,21,23]. Other envelope solutions of (4.24), such as $A_1=f(R)$ where $f(R)$ is a higher-mode solution (with nodes) or vortex-ring solutions $A_1=f(R)e^{in\Theta}$, could lead to other types of solitary wave structures.

Next, we consider point B. At this point, a single Bloch mode exists and has been shown in Fig. 4(b). This Bloch mode is located at the M point of the first Brillouin zone, is 2π periodic along both x and y directions, and its adjacent peaks are out of phase. The envelope equation at this point is given by (4.24) with the coefficients D_1 and α_0 given in Eq. (4.27). Since $D_1<0$, solitary waves will bifurcate into the first band gap ($\eta>0$) under a defocusing nonlinearity ($\sigma=-1$). If we take the solution of (4.24) to be the ground-state envelope solution, the corresponding analytical solution $u_0(x,y)$ is a gap soliton with nodes. Such solutions have been reported in [5,15,23].

The envelope solutions at points C, D, and E are richer and more interesting. Two of them, which are the so-called reduced-symmetry solitons [30] and gap vortex solitons [27], have been reported before. But many other solutions at these points have not been considered yet to our knowledge. They include solutions that we call dipole-array solitons, dipole-cell solitons, vortex-cell solitons, etc. Envelope solutions and the corresponding leading-order analytical solutions $u_0(x,y)$ at these three points will be described in the next three subsections, respectively.

A. Envelope solutions at point C

At point C, two Bloch modes exist. One of them is shown in Fig. 4(c), while the other is a 90° rotation of Fig. 4(c).

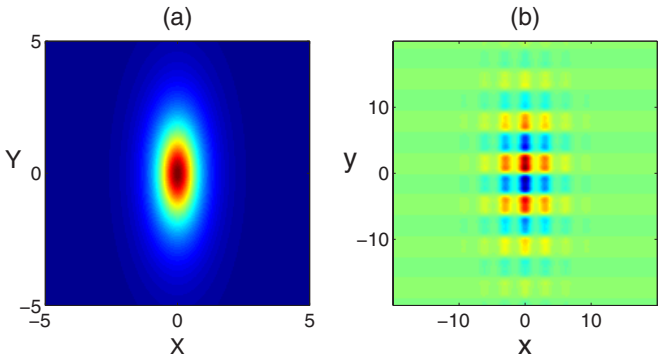

FIG. 5. (Color online) (a) Envelope solution $A_1(X,Y)$ at point C with $A_2=0$; (b) the corresponding analytical single-Bloch-mode soliton $u_0(x,y)$ with $\epsilon=0.2$.

These Bloch modes are located at the X and X' points of the first Brillouin zone. They are π periodic along one spatial direction, and 2π periodic along the other spatial direction. The envelope equations at this point are given by (4.16) and (4.17), with the coefficients D_1, D_2, α, β given in Eq. (4.21), and $\gamma=0$. Since $D_1, D_2>0$ here, solitary waves will bifurcate into the first band gap ($\eta<0$) under a focusing nonlinearity ($\sigma=1$). Since $\gamma=0$, we have three solution reductions (see above). Under these reductions, we consider the following subclasses of solutions.

(i) $A_1>0$, $A_2=0$. In this case, the envelope solution is an ellipse as shown in Fig. 5(a). This ellipse stretches along the Y direction. When the Bloch wave [see Fig. 4(c)] is modulated by this envelope function, the resulting leading-order analytical solution $u_0(x,y)$ is plotted in Fig. 5(b) (with ϵ taken as 0.2). This solution contains only a single Bloch mode (since $A_2=0$); thus we can call it a *single-Bloch-mode soliton*. This soliton is narrower along the x direction, and broader along the y direction; thus, it is expected to be more mobile along the y direction and less so along the x direction. This type of solution has been observed in [30] for a different (saturable) nonlinearity (see Sec. VI A for more details). In that paper, these solutions were called reduced-symmetry solitons. One of their potential applications in optical routing and switching has been described in [39].

(ii) $A_1>0$, $A_2>0$. In this case, the envelope solutions are both real and positive, and they are shown in Figs. 6(a) and 6(b). They are both ellipse shaped but stretched along opposite directions. The corresponding leading-order analytical solution $u_0(x,y)$ is plotted in Figs. 6(c) and 6(d) (with ϵ taken as 0.2). The central region of this solitary wave is a dipole array aligned along the two diagonal directions; thus, we will call this solitary wave a *dipole-array gap soliton*. The outer region of this soliton is aligned along the horizontal (x) and vertical (y) directions though. Note that this dipole-array soliton is quite different from dipole solitons reported before (see [19,26] for instance): previous dipole solitons reside in the semi-infinite band gap, and their peaks are at lattice sites; but the present dipole-array soliton resides in the first band gap, and its peaks are off lattice sites. This dipole-array gap soliton arises due to a superposition of two modulated Bloch modes [see Eq. (4.4)], and has not been reported before to our knowledge.

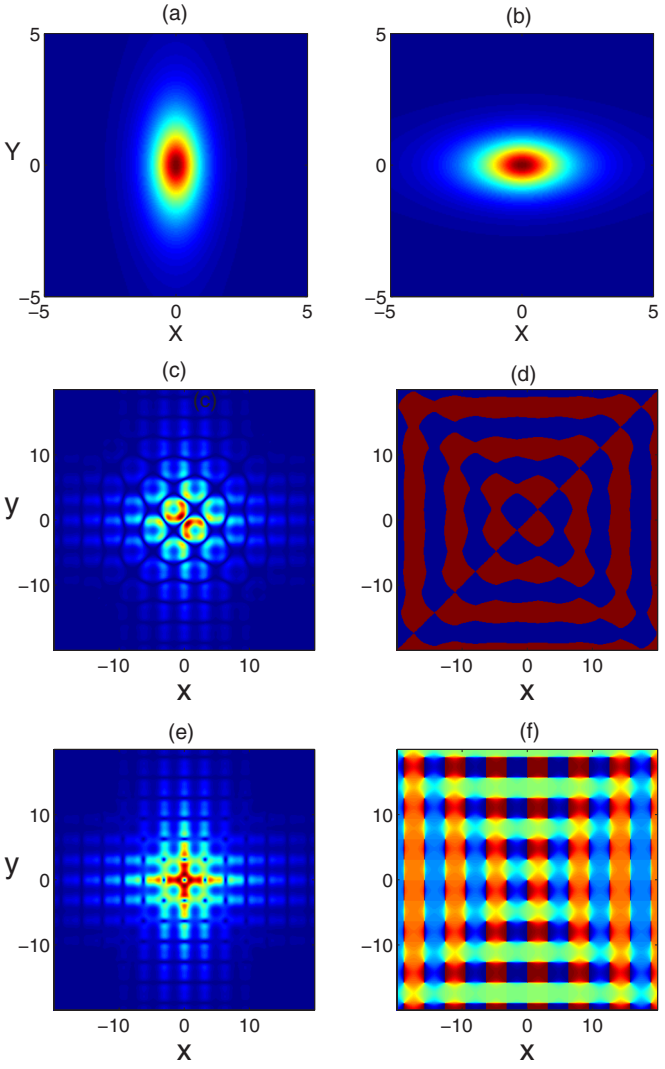

FIG. 6. (Color online) (a), (b) Envelope solutions $A_1(X,Y)>0$ (left) and $A_2(X,Y)>0$ (right) at point C; (c), (d) the corresponding analytical dipole-array soliton $u_0(x,y)$ with $\epsilon=0.2$: the left is the amplitude and right the phase; (e), (f) the analytical vortex-array soliton $u_0(x,y)$ at point C in the case (iii) with $\epsilon=0.2$: the left is the amplitude and right the phase.

(iii) $A_1>0$, $A_2=i\hat{A}_2$, $\hat{A}_2>0$. In this case, the envelope of one Bloch wave is real, while that of the other Bloch wave is purely imaginary. In the literature, two such Bloch modes are said to have $\pi/2$ phase delay [12,27]. Envelope functions A_1 and $\hat{A}_2$ look very similar to A_1 and A_2 of Figs. 6(a) and 6(b). Indeed, it is easy to see that A_1 and $\hat{A}_2$ satisfy the same equations as A_1 and A_2 of the previous reduction (ii), except that the β coefficient is slightly different. The leading-order analytical solution $u_0(x,y)$ for these envelope solutions is displayed in Figs. 6(e) and 6(f). This soliton looks quite different from the previous one in Figs. 6(c) and 6(d). The most significant difference is that, on winding around each lattice center (i.e., points $x=m\pi$, $y=n\pi$ with m,n being integers), the phase of the present soliton increases or decreases by 2π. In other words, the solution around each lattice center has a vortex structure. Thus, we call this solution a *vortex-array gap soliton*. This vortex-array soliton is qualitatively the

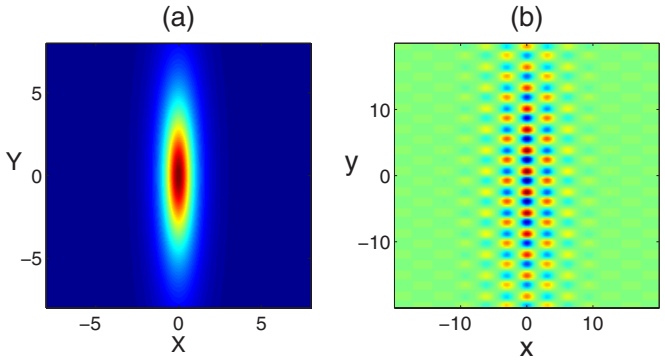

FIG. 7. (Color online) (a) Envelope solution $A_1(X,Y)$ at point D with $A_2=0$; (b) the corresponding analytical single-Bloch-mode soliton $u_0(x,y)$ with $\epsilon=0.2$.

same as the gap vortex soliton reported in [27] for a different nonlinearity (see Sec. VI A). However, it is quite different from the other vortex solitons residing inside the semi-infinite band gap, as has been reported in [21,22,24,25] before.

For a vortex-type soliton, its angular momentum is an important quantity. This momentum is defined as

$$\Omega \equiv \int \mathbf{r} \times \mathrm{Im}(\bar{u}\nabla u)d\mathbf{r} = \mathrm{Im}\int_{-\infty}^{\infty}\int_{-\infty}^{\infty} \bar{u}(xu_y - yu_x)dx\,dy. \tag{5.1}$$

Here $\mathrm{Im}(\bar{u}\nabla u)$ is the linear momentum, and $\mathbf{r}$ is the position vector in the (x,y) plane. The spin of the vortex is defined as

$$S = \frac{\Omega}{\int |u|^2 d\mathbf{r}}. \tag{5.2}$$

In the absence of the periodic potential, the spin of a vortex soliton takes an integer value equal to the phase winding number (topological charge). In the present case with a periodic potential, the spin of a vortex-array gap soliton does not take integer values in general. Even though this soliton has a local vortex structure around each lattice center, the topological charges of adjacent lattice centers are opposite; thus, the total spin of this vortex-array soliton is finite, not infinite. In fact, substituting the perturbation-series solution (4.2) and (4.4), and $A_1 \in \mathbb{R}$, $A_2 \in i\mathbb{R}$ into the Ω and S formulas, we can easily show that both Ω and S approach zero as $\epsilon \to 0$. Thus, the spin of these vortex-array solitons is quite small.

B. Envelope solutions at point D

Point D admits two Bloch waves, one shown in Fig. 4(d), and the other a 90° rotation of Fig. 4(d). These Bloch modes are located at the X and X' points of the first Brillouin zone. The envelope equations at this point are given by (4.16) and (4.17), with the coefficients D_1, D_2, α, β given in Eq. (4.22), and $\gamma=0$. Since $D_1, D_2 < 0$ now, solitary waves will bifurcate into the second band gap ($\eta > 0$) under a defocusing nonlinearity ($\sigma=-1$). As for point C, three solution reductions are admitted. Under these reductions, we consider the following subclasses of solutions.

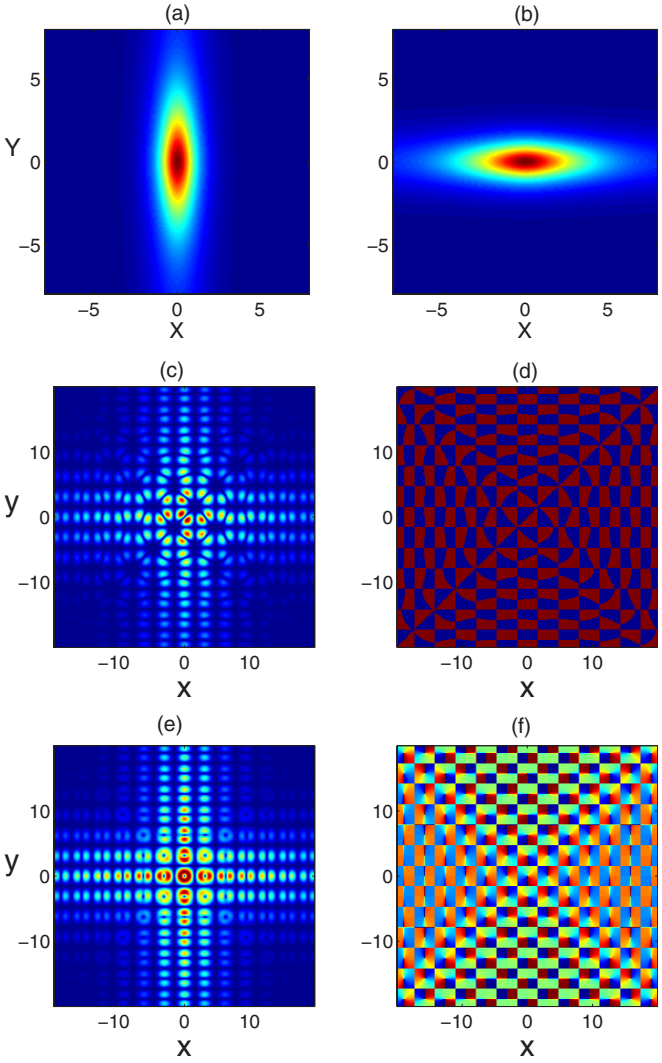

FIG. 8. (Color online) (a), (b) Envelope solutions $A_1(X,Y)>0$ (left) and $A_2(X,Y)>0$ (left) at point D; (c), (d) the corresponding analytical dipole-cell soliton $u_0(x,y)$ with $\epsilon=0.2$: the left is the amplitude and the right the phase; (e), (f) the analytical vortex-cell soliton $u_0(x,y)$ at point D in the case (iii) with $\epsilon=0.2$: the left is the amplitude and the right the phase.

(i) $A_1>0$, $A_2=0$. In this case, the envelope solution is an ellipse as shown in Fig. 7(a), which is thinner than Fig. 5(a) at point C. When the Bloch wave [see Fig. 4(d)] is modulated by this envelope function, the resulting leading-order analytical solution $u_0(x,y)$ is plotted in Fig. 7(b) (with $\epsilon=0.2$). This solution is also a single-Bloch-mode soliton since $A_2=0$. Due to the thin envelope solution, this soliton is much broader in the y direction than in the x direction. Thus, we can expect it to be much more mobile along the y direction than along the x direction. Note that this solution is under a defocusing nonlinearity, while a similar-looking solution in Fig. 5(b) (see also [30]) was under a focusing nonlinearity.

(ii) $A_1>0$, $A_2>0$. In this case, the envelope solutions are both real and positive and are shown in Figs. 8(a) and 8(b). They are both ellipse shaped, stretching along opposite directions. The corresponding leading-order analytical solution

$u_0(x,y)$ is plotted in Figs. 8(c) and 8(d) (with $\epsilon=0.2$). This solution looks quite different from its counterpart—the dipole-array soliton of Figs. 6(c) and 6(d) at point C. Its main feature is that the solution inside each lattice site is a dipole cell. Its difference from the dipole-array soliton at point C is that here, the two humps of each dipole are completely confined inside each individual lattice, while the two humps of each dipole in Figs. 6(c) and 6(d) spread to neighboring lattice sites. We will call this soliton in Figs. 8(c) and 8(d) a *dipole-cell gap soliton*. Solutions of this kind have not been reported before to our knowledge. Notice that in the central region of the soliton, dipole cells are aligned along diagonal directions, but in the outer region, dipole cells are dominant and aligned along the horizontal and vertical directions.

(iii) $A_1>0$, $A_2=i\hat{A}_2$, $\hat{A}_2>0$. In this case, the two Bloch modes have $\pi/2$ phase delay, and the envelope functions $(A_1,\hat{A}_2)$ are similar to (A_1,A_2) of Figs. 8(a) and 8(b). The leading-order analytical solution $u_0(x,y)$ with these envelope solutions is displayed in Figs. 8(e) and 8(f). The most significant feature of this solution is that, in the central region, the solution inside each lattice site is a vortex cell (with charge 1 or −1). Thus, we call it a *vortex-cell gap soliton*. The charges of adjacent cells are opposite; hence the total angular momentum and spin of this soliton are both finite. When $\epsilon\to 0$, the angular momentum and spin approach zero. Notice that each vortex cell here is completely isolated and confined inside each individual lattice, which is quite different from the vortex-array soliton in Figs. 6(e) and 6(f), where neighboring vortices are connected together and do not have clear-cut boundaries between them. In addition, this vortex-cell soliton is under a defocusing nonlinearity, while the vortex-array soliton of Figs. 6(e) and 6(f) was under a focusing nonlinearity (see also [27]). Furthermore, this vortex-cell soliton resides in the second band gap, while the vortex-array soliton of Figs. 6(e) and 6(f) resides in the first band gap. Gap vortex solitons under defocusing nonlinearity as reported in [15,29] reside also inside the first band gap; they are the counterparts of vortex solitons in the semi-infinite band gap as reported in [21,22], and are fundamentally different from the vortex-cell solitons bifurcated from point D here. Although these vortex-cell gap solitons have not been studied before, they do resemble the linear vortex-cell defect modes in photonic lattices as reported in [12].

C. Envelope solutions at point E

Point E also admits two Bloch modes, one shown in Fig. 4(e), and the other a 90° rotation of Fig. 4(e). These Bloch modes are both located at the Γ point of the first Brillouin zone and thus are π periodic along both spatial directions. The envelope equations at this point are given by (4.16) and (4.17), with the coefficients $D_1,D_2,\alpha,\beta,\gamma$ given in Eq. (4.23). Since $D_1,D_2>0$, solitary waves will bifurcate into the second band gap ($\eta<0$) under a focusing nonlinearity ($\sigma=1$). Since $\gamma\neq 0$, the reduction of $A_1,A_2\in\mathbb{R}$ is allowed, and we consider the following two subclasses of solutions.

(i) $A_1>0$, $A_2>0$. In this case, the envelope solutions are both real and positive, and they are shown in Figs. 9(a) and 9(b). They are both very thin ellipses stretched along opposite directions. The corresponding leading-order analytical solution $u_0(x,y)$ is plotted in Fig. 9(c) (with ϵ taken as 0.2). This solution has a pronounced cross-shaped overall structure. In the central region of the (x,y) plane, the solution at each lattice center is an almost circular positive spike, which recedes to negative backgrounds away from the lattice center. Thus, we may call this solution a spike-array gap soliton.

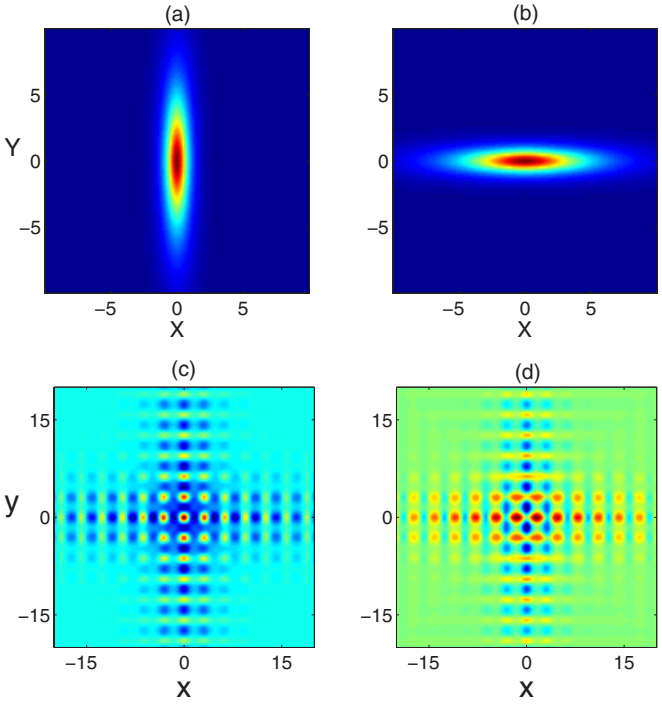

FIG. 9. (Color online) (a), (b) Envelope solutions $A_1(X,Y)>0$ (left) and $A_2(X,Y)>0$ (right) at point E; (c) the corresponding analytical spike-array soliton $u_0(x,y)$ with $\epsilon=0.2$; (d) the analytical quadrupole-array soliton $u_0(x,y)$ at point E in the case (ii) with $\epsilon=0.2$.

(ii) $A_1>0$, $A_2<0$. In this case, the envelope functions A_1 and $|A_2|$ are similar to those of Figs. 9(a) and 9(b), and thus not shown. The corresponding leading-order analytical solution $u_0(x,y)$ is plotted in Fig. 9(d) (with $\epsilon=0.2$). This solution also has a pronounced cross shape. In its central region, the solution resembles an array of quadrupoles; thus, we can call this solution a quadrupole-array gap soliton.

VI. FAMILIES OF SOLITARY WAVES BIFURCATED FROM BAND EDGES

The above multiscale perturbation analysis predicts various types of low-amplitude solitary waves when the propagation constant μ is near edges of Bloch bands. As the propagation constant moves away from band edges, these solitary waves will become more localized, and their amplitudes will increase. From an experimental point of view, more localized solitary waves are often easier to observe. For more localized solutions, the above perturbation analysis starts to break down, and numerical methods need to be employed. In this section, we compute whole families of solitary waves bifurcated from edges of Bloch bands. The nu-

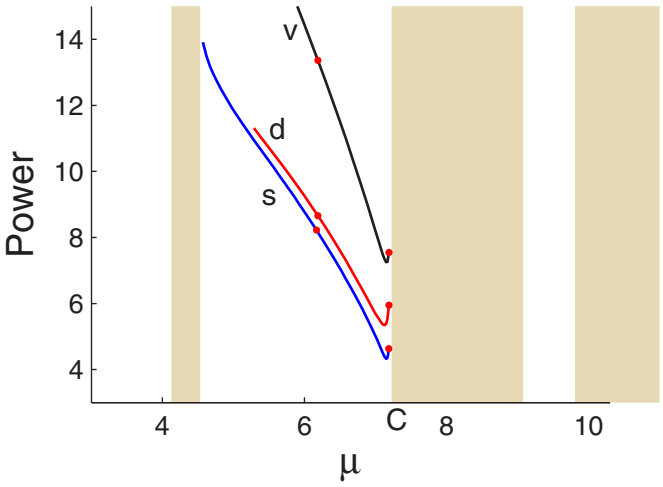

FIG. 10. (Color online) Power diagrams of the three families of solitary waves bifurcated from the edge point C (under focusing nonlinearity). Bottom curve, single-Bloch-mode branch (marked by letter "s"); middle curve, dipole-array branch (marked by letter "d"); top curve, vortex-array branch (marked by letter "v"). The marked thick dot points are 0.04 and 1.04 below the band edge C.

merical method we will use is the modified squared-operator iteration method developed in [35].

For illustration purpose, we determine families of solutions bifurcated from points C, D, and E of Fig. 3(b). Leading-order analytical approximations on low-amplitude solutions of these families have been presented in Figs. 5–9. Note that solution families bifurcated from points A and B have been reported before in [15,21,23]; thus, they will not be computed in this paper.

A. Solution families bifurcated from point C

At point C, three types of solitary waves have been predicted in the previous section under a focusing nonlinearity: single-Bloch-mode solitons, dipole-array solitons, and vortex-array solitons [see Figs. 5(b) and 6(c)–6(f), respectively]. They all exist in the first band gap, bifurcated from the edge point C of the second Bloch band. Numerically, we have obtained the entire families of these three types of solutions. Their power curves are displayed in Fig. 10. Here the power is defined as

$$P = \int_{-\infty}^{\infty} \int_{-\infty}^{\infty} |u(x,y)|^2 dx\, dy. \tag{6.1}$$

All the three power curves are nonmonotonic. They have nonzero minimum values inside the band gap, below which solitary waves of the corresponding family do not exist. This contrasts with the 1D case where solitary waves exist at all power levels [20]. Of these three power curves, the one for the single-Bloch-mode family is the lowest. Thus single-Bloch-mode solitons take the least power amount to excite. Solitary waves of all three families at $\mu=7.189$ and 6.189, which are 0.04 and 1.04 below the edge point C (where $\mu_0=7.229$), are plotted in Fig. 11. Note that the shorter separation $\mu-\mu_0=-0.04$ is chosen so that $\mu-\mu_0=-\epsilon^2$, where $\epsilon=0.2$ is the value we have used when plotting all analytical solutions $u_0(x,y)$ in Figs. 5 and 6. The solitons at $\mu=7.189$, shown in Figs. 11(a), 11(c), and 11(f), are weakly localized and have low amplitudes, and they are close to the band edge C. These numerical solutions are almost identical to the analytical ones shown in Figs. 5(b), 6(c), and 6(e) [the phase fields of solitons in Figs. 11(c) and 11(f) are also almost identical to the analytical ones in Figs. 6(d) and 6(f) and thus are not shown]. Thus, the numerical results corroborate the analytical theory of the previous section. More significant solutions in Fig. 11 are the three solitons at the other propagation constant $\mu=6.189$, which is deep inside the first band gap. These solutions, displayed in Figs. 11(b), 11(d), 11(e), 11(g), and 11(h), are strongly localized. Indeed, the soliton of the single-Bloch-mode family in Fig. 11(b) almost becomes a single dipole aligned along the y axis at the lattice site of origin $(x,y)=(0,0)$; the soliton of the dipole-array family in Figs. 11(d) and 11(e) almost becomes a single dipole aligned along the $y=-x$ direction at the lattice site of origin; and the soliton of the vortex-array family in Figs. 11(g) and 11(h) almost becomes a single vortex at the lattice site of origin.

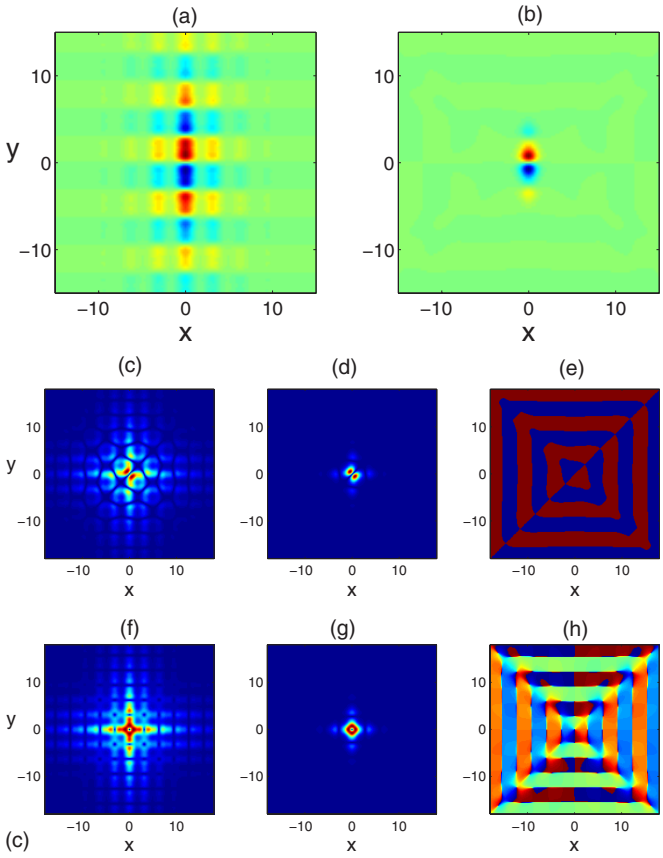

FIG. 11. (Color online) Weakly and strongly localized solutions on the three soliton branches bifurcated from the edge point C in Fig. 10. Propagation constants of these solutions are $\mu=6.189$ and 7.189, which are marked by thick dots in Fig. 10. Top row: single Bloch-mode solitons; $u(x,y)$ is shown; $\mu=$(a) 7.189; (b) 6.189. Middle and bottom rows: dipole-array and vortex-array solitons, respectively; (c), (f) amplitudes ($|u(x,y)|$) at $\mu=7.189$; (d), (e) amplitude and phase of the dipole-array soliton at $\mu=6.189$; (g), (h) amplitude and phase of the vortex-array soliton at $\mu=6.189$.

The phase structures of these strongly localized solitons, however, still resemble those of weakly localized ones [see Figs. 6(d), 6(f), 11(e), and 11(h)]. This strong localization of solitons in these solution families makes them useful for on-axis excitation in photorefractive crystals. Indeed, the soliton of vortex-array family in Figs. 11(g) and 11(h) looks almost identical to the gap vortex soliton observed in [27] with on-axis excitation. It should be noted that reduced-symmetry solitons observed in [30] also bifurcate from single Bloch modes at point C. However, such solitons observed in [30] at high powers look a little different from that in Fig. 11(b): their solitons are confined to three lattice sites, with the middle-site peak intensity higher than those at the two neighboring sites; while the soliton of Fig. 11(b) is confined to two lattice sites with equal peak intensities. The reason for this difference is the following. As we have explained in Sec. IV B, the envelopes of Bloch modes can be centered at four locations [see Eq. (4.44)]. For the single-Bloch-mode soliton family shown in Figs. 10, 11(a), and 11(b), the envelope was centered at the origin $(x_0, y_0)=(0,0)$, which leads to a dipole structure under strong localization. If the envelope is centered at $(x_0, y_0)=(0, L/2)=(0, \pi/2)$ instead, solitons under strong localizations would have a central peak shouldered by two equal but lower-intensity peaks just like those observed in [30]. Thus, the solitons observed in [30] belong to the single-Bloch-mode soliton family of point C with the envelope centered at $(0, \pi/2)$ rather than (0,0). From the experimental point of view, dipole-array solitons as shown in Figs. 11(c)–11(e), as well as the strongly localized single-Bloch-mode soliton of dipole type in Fig. 11(b), have never been observed before to our knowledge, and they still await experimental demonstration.

B. Solution families bifurcated from point D

At point D, three types of solitary waves were predicted in Sec. V under a defocusing nonlinearity: single-Bloch-mode solitons, dipole-cell solitons, and vortex-cell solitons [see Figs. 7(b) and 8(c)–8(f) respectively]. They all exist in the second band gap, bifurcated from the edge point D of the second Bloch band. Numerically, we have obtained the entire families of these three types of solutions. Their power curves are displayed in Fig. 12. These power curves are also nonmonotonic and have nonzero minimum values inside the band gap. Solitary waves of these three families at $\mu=9.121$ and 9.621, which are 0.04 and 0.54 above the edge point D (where $\mu_0=9.081$), are plotted in Fig. 13. The solitons at $\mu=9.121$, shown in Figs. 13(a), 13(c), and 13(f), are weakly localized and have low amplitudes. They are located close to the band edge D. These numerical solutions are almost indistinguishable from the analytical ones shown in Figs. 7(b), 8(c), and 8(e) where $\epsilon=0.2$ [the phase fields of solitons in Figs. 13(c) and 13(f) are also almost indistinguishable from the analytical ones in Figs. 8(d) and 8(f) and thus are not shown]; thus, numerical and analytical solutions near the band edge D are in agreement. Solutions at $\mu=9.621$ away from the edge point D are more localized. These solutions are displayed in Figs. 13(b), 13(d), 13(e), 13(g), and 13(h), respectively. The single-Bloch-mode soliton in Fig. 13(b) is confined to only one lattice site along the x direction, but occupies quite a few lattice sites along the y direction. Thus, this soliton will be highly mobile along the y direction and strongly trapped along the x direction. The dipole-cell soliton in Figs. 13(d) and 13(e) is largely confined to the single lattice site at the origin as a dipole aligned along the $y=-x$ direction, with long tails stretching along the horizontal and vertical (i.e., lattice) directions in a cross pattern. The vortex-cell soliton in Figs. 13(g) and 13(h) is also largely confined to the single lattice site at the origin in the form of a vortex ring with charge −1, with long tails along the horizontal and vertical axes as well. None of these solitary wave structures in Fig. 13 was theoretically predicted or experimentally observed before to our knowledge. These structures exist under a defocusing nonlinearity. Such nonlinearity can be obtained in photorefractive crystals with a negative bias charge or in Bose-Einstein condensates for certain types of atoms such as ^{87}Rb and ^{23}Na [14].

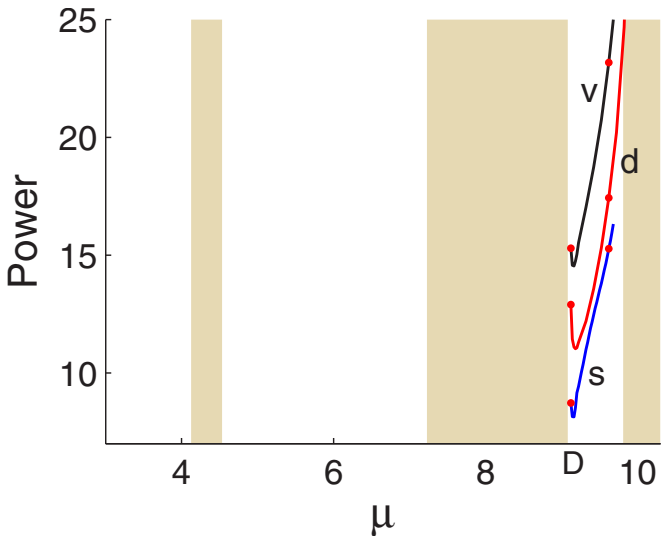

FIG. 12. (Color online) Power diagrams of the three families of solitary waves bifurcated from the edge point D (under a defocusing nonlinearity). Bottom curve, single-Bloch-mode branch (marked by letter "s"); middle curve, dipole-cell branch (marked by letter "d"); top curve, vortex-cell branch (marked by letter "v"). The marked thick dot points are 0.04 and 0.54 above the band edge D.

C. Solution families bifurcated from point E

At point E, two types of solitary waves were predicted in Sec. V under a focusing nonlinearity: spike-array solitons and quadrupole-array solitons [see Figs. 9(c) and 9(d)]. They exist in the second band gap, bifurcated from the edge point E of the third Bloch band. Numerically, we have obtained families of these two types of solutions. Their power curves are displayed in Fig. 14. These power curves are also nonmonotonic and have nonzero minimum values inside the band gap. Solitary waves of these families at $\mu=9.77$ and 9.33, which are 0.04 and 0.48 above the edge point E (where $\mu_0=9.81$), are plotted in Fig. 15. The solitons at $\mu=9.77$, shown in Figs. 15(a) and 15(c), are weakly localized and have low amplitudes. They are almost the same as the ana-

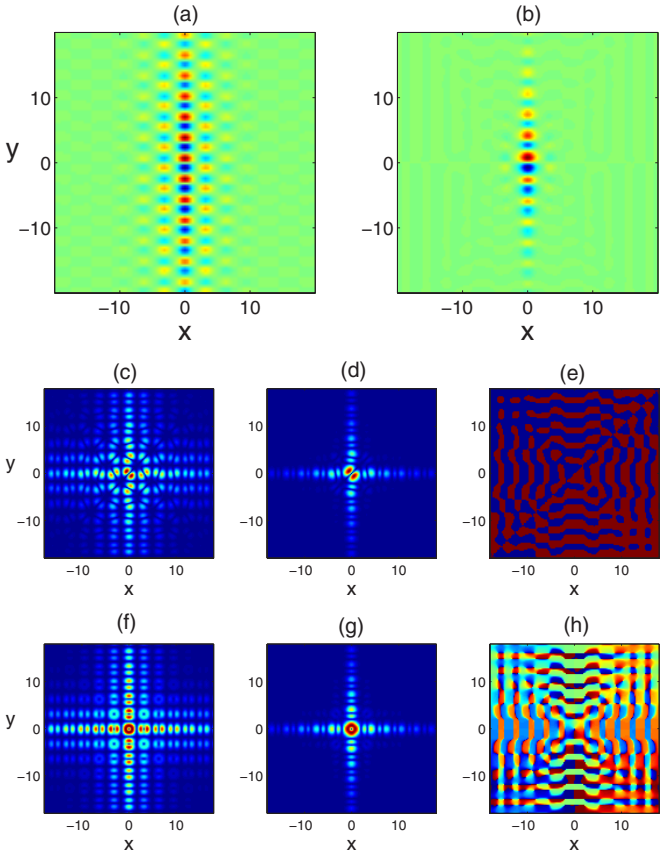

FIG. 13. (Color online) Weakly and strongly localized solutions on the three soliton branches bifurcated from the edge point D in Fig. 12. Propagation constants of these solutions are μ=9.121 and 9.621, which are marked by thick dots in Fig. 12. Top row: single Bloch-mode solitons; $u(x,y)$ is shown; μ=(a) 9.121; (b) 9.621. Middle and bottom rows: dipole-cell and vortex-cell solitons respectively; (c), (f) amplitudes ($|u(x,y)|$) at μ=9.121; (d), (e) amplitude and phase of the dipole-cell soliton at μ=9.621; (g), (h) amplitude and phase of the vortex-cell soliton at μ=9.621.

lytical solutions in Figs. 9(c) and 9(d) where ϵ=0.2, which is expected. The solutions at μ=9.33 away from the edge point E are more localized. These solutions are displayed in Figs. 15(b) and 15(d). The localized solution of the spike-array soliton family in Fig. 15(b) is now confined to only a few lattice sites on the x and y axes, with a dominant circular spike in its center. The localized solution of the quadrupole-array soliton family in Fig. 15(d) is confined also to only a few lattice sites on the x and y axes, with a quadrupole in its center. These types of solitary waves have not been reported before to our knowledge.

VII. TIME-DEPENDENT ENVELOPE EQUATIONS

In the previous sections, our focus was to obtain solitary waves in Eq. (2.1); thus, our envelope equations (4.16), (4.17), and (4.24) were time independent. If we look beyond solitary waves, we can further study how slowly modulated low-amplitude Bloch-wave packets evolve with time under nonlinear effects. In such a study, envelope equations of Bloch modes will be time dependent. Such time-dependent

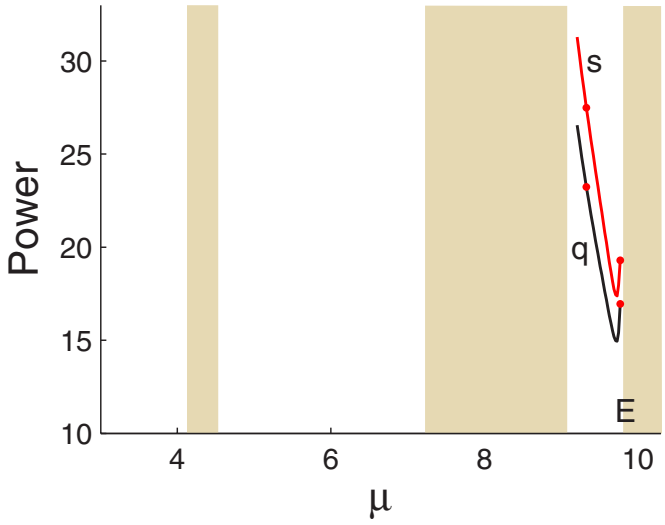

FIG. 14. (Color online) Power diagrams of the two families of solitary waves bifurcated from the edge point E (under focusing nonlinearity). Upper curve, the spike-array branch (marked by letter "s"); lower curve, the quadrupole-array branch (marked by letter "q"). The marked thick dot points are 0.04 and 0.48 below the band edge E.

envelope equations are essential not only for the tracking of Bloch-wave packet movements, but also for the stability analysis of stationary envelope solutions obtained in Sec. V. This is analogous to the role the nonlinear Schrödinger equa-

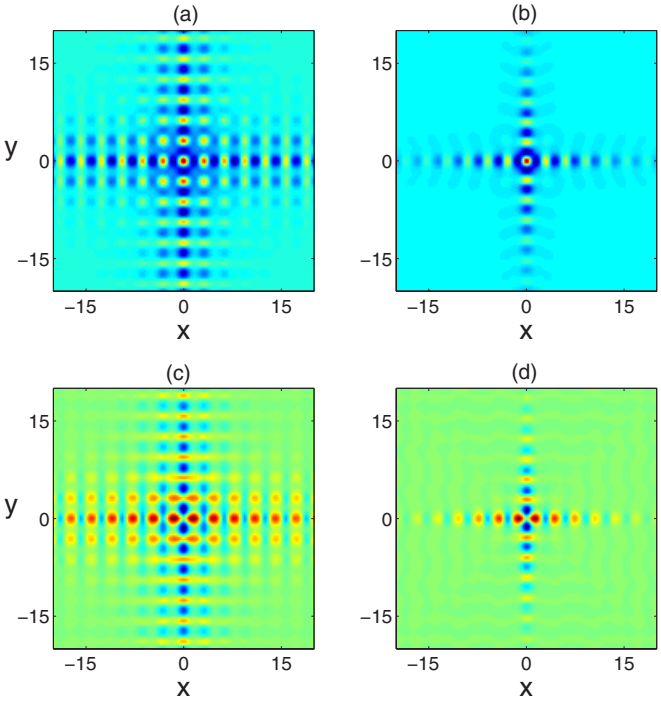

FIG. 15. (Color online) Weakly and strongly localized solutions on the two soliton branches bifurcated from the edge point E in Fig. 14. Upper row, spike-array solitons; lower row, quadrupole-array solitons. Propagation constants of these solutions are μ=9.77 (left column) and 9.33 (right column), which are marked by thick dots in Fig. 14.

tion played in the study of water wave packets and light pulses in nonlinear optics [40,41]. The derivation of time-dependent envelope equations is a simple extension of the analysis in Sec. IV and will be performed briefly below. As before, the derivation will be carried out for the slightly more complicated case where the solution is near band edges with two different Bloch modes. Results for the simpler case of the solution being near band edges with a single Bloch mode will be given without elaboration.

Consider the evolution of low-amplitude Bloch-wave packets in Eq. (2.1) near a band edge $\mu=\mu_0$ with two different Bloch modes $p_1(x)p_2(y)$ and $p_2(x)p_1(y)$. The solution can be expanded into the following perturbation series:

$$U(x,y,t) = e^{-i\mu_0 t}(\epsilon U_0 + \epsilon^2 U_1 + \epsilon^3 U_2 + \cdots), \tag{7.1}$$

where

$$U_0 = A_1(X,Y,T)p_1(x)p_2(y) + A_2(X,Y,T)p_2(x)p_1(y), \tag{7.2}$$

$\epsilon \ll 1$, $X=\epsilon x$, $Y=\epsilon y$ are slow spatial variables, and $T=\epsilon^2 t$ is the slow time variable. When this expansion is substituted into Eq. (2.1), we find at $O(\epsilon^2)$ that the equation for U_1 is simply Eq. (4.5) with u_k $(k=0,1)$ replaced by U_k, and with an additional term $i\partial U_1/\partial t$ added onto its left-hand side. The solution for U_1 is still given by Eq. (4.8). At $O(\epsilon^3)$, we find that the equation for U_2 is Eq. (4.11) with u_k $(k=0,1,2)$ replaced by U_k, with an additional term $i\partial U_2/\partial t$ added onto its left-hand side, and with ηu_0 replaced by $i\partial U_0/\partial T$. Requiring the U_2 solution to not grow linearly with time t (suppression of secular terms), the following time-dependent equations will be derived for the envelope functions $A_1(X,Y,T)$ and $A_2(X,Y,T)$:

$$i\frac{\partial A_1}{\partial T} + D_1\frac{\partial^2 A_1}{\partial X^2} + D_2\frac{\partial^2 A_1}{\partial Y^2} + \sigma[\alpha|A_1|^2 A_1 + \beta(\bar{A}_1 A_2^2 + 2A_1|A_2|^2) + \gamma(|A_2|^2 A_2 + \bar{A}_2 A_1^2 + 2A_2|A_1|^2)] = 0, \tag{7.3}$$

$$i\frac{\partial A_2}{\partial T} + D_2\frac{\partial^2 A_2}{\partial X^2} + D_1\frac{\partial^2 A_2}{\partial Y^2} + \sigma[\alpha|A_2|^2 A_2 + \beta(\bar{A}_2 A_1^2 + 2A_2|A_1|^2) + \gamma(|A_1|^2 A_1 + \bar{A}_1 A_2^2 + 2A_1|A_2|^2)] = 0. \tag{7.4}$$

Here all coefficients D_1, D_2, α, β, and γ are the same as those given in Eqs. (4.15) and (4.18)–(4.20).

If the solution of Eq. (2.1) is a low-amplitude Bloch-wave packet near a band edge $\mu=\mu_0$ where a single Bloch mode $p_1(x)p_1(y)$ exists, the perturbation expansion for the solution U is still Eq. (7.1), except that

$$U_0 = A_1(X,Y,T)p_1(x)p_1(y) \tag{7.5}$$

now. In this case, the equation for the envelope function $A_1(X,Y,T)$ reduces to

$$i\frac{\partial A_1}{\partial T} + D_1\left(\frac{\partial^2 A_1}{\partial X^2} + \frac{\partial^2 A_1}{\partial Y^2}\right) + \sigma\alpha_0|A_1|^2 A_1 = 0, \tag{7.6}$$

where the coefficients D_1 and α_0 are given in Eqs. (4.15) and (4.25).

Using the above time-dependent envelope equations, one can study the time evolution of Bloch-wave packets. In addition, one can analyze linear and nonlinear stabilities of stationary Bloch-wave packet solutions [i.e., solitary waves in Eqs. (7.3), (7.4), and (7.6)]. Such studies lie outside the scope of the present paper.

VIII. SUMMARY AND DISCUSSION

In this paper, we systematically studied various families of solitary waves which are bifurcated from Bloch-band edges in the two-dimensional NLS equation with a periodic potential. Near the band edges, we analytically derived envelope equations for low-amplitude Bloch-wave packets. Based on these envelope equations, many types of solitary waves inside band gaps were predicted, including dipole-array solitons, dipole-cell solitons, vortex-cell solitons, etc. Away from the band edges, solitary waves were traced numerically, and strongly localized solitary waves of the corresponding families were obtained. These solitary waves have distinctive intensity and phase patterns such as cross-shape intensity distributions and vortex-cell phase profiles. Certain solitary waves previously reported in 2D photonic lattices such as reduced-symmetry solitons [30] and gap vortex solitons [27] were found to be special cases of our general classes of solutions.

In this paper, the relatively simple and obvious types of solutions in envelope equations were determined, and their induced solitary wave families computed. Whether other solutions of envelope equations would generate additional families of solitary waves is still an open question. For instance, the single-envelope equation (4.24) also admits vortex-ring solutions of the type $f(R)e^{in\Theta}$. Whether such solutions would lead to new families of vortex-type lattice solitons remains to be seen. For the coupled envelope equations (4.16) and (4.17), it is not even clear what kind of additional solutions they admit beyond the ones we presented in this paper. Thus, a classification of solutions in the coupled envelope equations (4.16) and (4.17) is highly desirable. The linear and nonlinear stability of solitary waves reported in this paper is another open question which merits careful investigation. From the experimental point of view, the challenge is to experimentally demonstrate the types of solitary waves obtained in this paper, such as dipole-array solitons and vortex-cell solitons. These open questions are beyond the scope of the present paper, and will be left for future studies.

ACKNOWLEDGMENTS

The authors appreciate helpful discussions with Dr. Zhigang Chen. This work was partially supported by the Air Force Office of Scientific Research under Grant No. USAF 9550-05-1-0379.

[1] J. D. Joannopoulos, R. D. Meade, and J. N. Winn, *Photonic Crystals: Molding the Flow of Light* (Princeton University Press, Princeton, NJ, 1995).
[2] P. Russell, Science **299**, 358 (2003).
[3] H. S. Eisenberg, Y. Silberberg, R. Morandotti, A. R. Boyd, and J. S. Aitchison, Phys. Rev. Lett. **81**, 3383 (1998).
[4] Z. Chen and K. McCarthy, Opt. Lett. **27**, 2019 (2002).
[5] J. W. Fleischer, M. Segev, N. K. Efremidis, and D. N. Christodoulides, Nature (London) **422**, 147 (2003).
[6] M. Petrovic, D. Trager, A. Strinic, M. Belic, J. Schröder, and C. Denz, Phys. Rev. E **68** 055601(R) (2003).
[7] H. Martin, E. D. Eugenieva, Z. Chen, and D. N. Christodoulides, Phys. Rev. Lett. **92**, 123902 (2004).
[8] R. Iwanow, R. Schiek, G. I. Stegeman, T. Pertsch, F. Lederer, Y. Min, and W. Sohler, Phys. Rev. Lett. **93**, 113902 (2004).
[9] U. Peschel, R. Morandotti, J. S. Aitchison, H. S. Eisenberg, and Y. Silberberg, Appl. Phys. Lett. **75** 1348 (1999).
[10] F. Fedele, J. Yang, and Z. Chen, Opt. Lett. **30**, 1506 (2005).
[11] F. Fedele, J. Yang, and Z. Chen, Stud. Appl. Math. **115**, 279 (2005).
[12] I. Makasyuk, Z. Chen, and J. Yang, Phys. Rev. Lett. **96**, 223903 (2006).
[13] X. Wang, J. Young, Z. Chen, D. Weinstein, and J. Yang, Opt. Express **14**, 7362 (2006).
[14] F. Dalfovo, S. Giorgini, L. P. Pitaevskii, and S. Stringari, Rev. Mod. Phys. **71**, 463 (1999).
[15] E. Ostrovskaya and Y. S. Kivshar, Opt. Express **12**, 19 (2004).
[16] Th. Anker, M. Albiez, R. Gati, S. Hunsmann, B. Eiermann, A. Trombettoni, and M. K. Oberthaler, Phys. Rev. Lett. **94**, 020403 (2005).
[17] D. N. Christodoulides and R. I. Joseph, Opt. Lett. **13**, 794 (1988).
[18] J. W. Fleischer, T. Carmon, M. Segev, N. K. Efremidis, and D. N. Christodoulides, Phys. Rev. Lett. **90**, 023902 (2003).
[19] D. Neshev, E. Ostrovskaya, Yu. S. Kivshar, and W. Krolikowski, Opt. Lett. **28**, 710 (2003).
[20] D. E. Pelinovsky, A. A. Sukhorukov, and Y. S. Kivshar, Phys. Rev. E **70**, 036618 (2004).
[21] J. Yang and Z. H. Musslimani, Opt. Lett. **23**, 2094 (2003).
[22] B. B. Baizakov, B. A. Malomed, and M. Salerno, Europhys. Lett. **63**, 642 (2003).
[23] N. K. Efremidis, J. Hudock, D. N. Christodoulides, J. W. Fleischer, O. Cohen, and M. Segev, Phys. Rev. Lett. **91**, 213906 (2003).
[24] D. N. Neshev, T. J. Alexander, E. A. Ostrovskaya, Y. S. Kivshar, H. Martin, and Z. Chen, Phys. Rev. Lett. **92**, 123903 (2004).
[25] J. W. Fleischer, G. Bartal, O. Cohen, O. Manela, M. Segev, J. Hudock, and D. N. Christodoulides, Phys. Rev. Lett. **92**, 123904 (2004).
[26] J. Yang, I. Makasyuk, A. Bezryadina, and Z. Chen, Stud. Appl. Math. **113**, 389 (2004).
[27] G. Bartal, O. Manela, O. Cohen, J. W. Fleischer, and M. Segev, Phys. Rev. Lett. **95**, 053904 (2005).
[28] H. Buljan, G. Bartal, O. Cohen, T. Schwartz, O. Manela, T. Carmon, M. Segev, J. W. Fleischer, and D. N. Christodoulides, Stud. Appl. Math. **115**, 173208 (2005).
[29] H. Sakaguchi and B. A. Malomed, J. Phys. B **37**, 2225 (2004).
[30] R. Fischer, D. Trager, D. N. Neshev, A. A. Sukhorukov, W. Krolikowski, C. Denz, and Y. S. Kivshar, Phys. Rev. Lett. **96**, 023905 (2006).
[31] D. Trger, R. Fischer, D. N. Neshev, A. A. Sukhorukov, C. Denz, W. Krlikowski, and Y. S. Kivshar, Opt. Express **14**, 1913 (2006).
[32] Y. V. Kartashov, V. A. Vysloukh, and L. Torner, Phys. Rev. Lett. **93**, 093904 (2004).
[33] X. Wang, Z. Chen, and P. G. Kevrekidis, Phys. Rev. Lett. **96**, 083904 (2006).
[34] M. J. Ablowitz, B. Ilan, E. Schonbrun, and R. Piestun, Phys. Rev. E **74**, 035601(R) (2006).
[35] J. Yang and T. I. Lakoba, Stud. Appl. Math. **118**, 153 (2007).
[36] J. Yang, New J. Phys. **6**, 47 (2004).
[37] B. B. Baizakov, V. V. Konotop, and M. Salerno, J. Phys. B **35**, 5105 (2002).
[38] T. S. Yang and T. R. Akylas, J. Fluid Mech. **330**, 215 (1997).
[39] D. N. Christodoulides and E. D. Eugenieva, Phys. Rev. Lett. **87**, 233901 (2001).
[40] D. J. Benney and G. J. Roskes, Stud. Appl. Math. **48**, 377 (1969).
[41] A. Hasegawa and Y. Kodama, *Solitons in Optical Communications* (Clarendon, Oxford, 1995).